Journal of
Materials Chemistry A

Materials for energy and sustainability

Accepted Manuscript

This article can be cited before page numbers have been issued, to do this please use: C. Huang, Y. Lai, Y. Huang, Y. L. Tsai, K. Limwatcharagul, M. E. Ashebir, H. Wu, M. Hayashi, M. Qorbani, K. H. Chen and L. Chen, *J. Mater. Chem. A*, 2026, DOI: 10.1039/D5TA10187E.

This is an Accepted Manuscript, which has been through the Royal Society of Chemistry peer review process and has been accepted for publication.

Accepted Manuscripts are published online shortly after acceptance, before technical editing, formatting and proof reading. Using this free service, authors can make their results available to the community, in citable form, before we publish the edited article. We will replace this Accepted Manuscript with the edited and formatted Advance Article as soon as it is available.

You can find more information about Accepted Manuscripts in the Information for Authors.

Please note that technical editing may introduce minor changes to the text and/or graphics, which may alter content. The journal's standard Terms & Conditions and the Ethical guidelines still apply. In no event shall the Royal Society of Chemistry be held responsible for any errors or omissions in this Accepted Manuscript or any consequences arising from the use of any information it contains.

ROYAL SOCIETY OF CHEMISTRY

rsc.li/materials-a

View Article Online
DOI: 10.1039/D5TA10187E

Journal of

Materials Chemistry A

ARTICLE

Selection of single-atom for surface charge modulation to promote CO_2 activation and stabilize *COOH intermediate for solar fuels

Received 00th January 20xx,
Accepted 00th January 20xx

DOI: 10.1039/x0xx00000x

Chih-Yang Huang[a, b, c], Ying-Ren Lai[c, d], Yi-Fan Huang[e], Tsai-Yu Lin[a, b, c], Kongpop Limwatcharagul[a, b, c], Mengstu Etay Ashebir[c, f, g, h, i], Heng-Liang Wu[c, d, j], Michitoshi Hayashi[c ,d]*, Mohammad Qorbani[k, l]*, Kuei-Hsien Chen[c, i]* and Li-Chyong Chen[c, d, m]*

Modulating surface charge distribution is a key strategy for enhancing photocatalytic CO_2 reduction, as it effectively activates the inert CO_2 molecule into a reactive, bent configuration. However, the rational design of such catalysts is fundamentally challenged by the lack of a systematic, predictive guideline for selecting optimal anchored single metal atoms. We address this critical gap by establishing a novel predictive metal selection principle based on the synergistic effect of the single atom's valence electron count and electronegativity. This principle successfully guided the selection of transition metals (Cr, Fe, Ni) anchored onto WO_3 nanoplates via wet impregnation, ensuring selective surface modification while preserving bulk properties. The Fe-anchored WO_3 catalyst, identified by our principle, demonstrated the most substantial surface electron density localization. This rational optimization led to a remarkable three-fold enhancement in PC-CO_2RR efficiency, selectively yielding CO as the primary product. Comprehensive experimental and theoretical analyses confirmed that this localized charge accumulation promotes significantly stronger CO_2 chemisorption and critically stabilizes the *COOH key intermediate. Specifically, the reaction became thermodynamically spontaneous with ΔG(*COOH) = -1.73 eV. Our findings establish a strong correlation between localized surface charge density and CO_2 activation, providing a fundamental and generalizable guideline for the rational design of high-performance catalytic materials for energy and sustainability applications.

Introduction

Global warming has been a concern for several decades, leading to serious environmental problems such as rising mean surface temperature, sea levels, and climate change.[1] In particular, carbon dioxide (CO_2) is one of the most threatening greenhouse gases due to its massive emissions from human activities, which may cause serious or irreversible damage.[2] As one of the alternative solutions, photocatalytic CO_2 reduction reaction (PC-CO_2RR) has attracted attention, which can convert CO_2 into valuable fuels (such as CO and CH_4) using sustainable solar energy.[3-6] However, PC-CO_2RR is limited by its low conversion efficiency due to chemically inert nature of the linear configuration of the CO_2 molecule.[7] According to the literatures, the adsorption of CO_2 on the surface active sites is a critical step, which plays a significant role in influencing the reduction reaction pathways, and ultimately determining the PC productivity and selectivity of PC processes.[3, 8] While intrinsic defects, grain boundaries, and edges are recognized as active sites for CO_2RR, activating CO_2 on the inert basal plane or the surface atomic structure of the catalyst is more advantageous.[9-11] Therefore, re-designing a catalyst's surface to enhance product yield is essential for pursuing high conversion efficiency.

In the realm of photocatalysis, the arrangement of atoms on the surface is momentous due to its substantial impact on surface electron density distribution for catalytic activity and selectivity.[12-14] For instance, charge-enriched dual metal site catalyst, *e.g.*, V_S-$CuIn_5S_8$, alters the CO_2 adsorption mode from weak M–C or M–O bonds to stronger M–C–O–M bonds. This alteration allows CO_2 to remain on the catalyst surface longer, awaiting the subsequent protonation step all the way to yield CH_4.[12] Generally, the localized surface electron density enables CO_2 adsorption through orbital hybridization between C or O and surface atoms.[13, 15-16] Several

[a] International Graduate Program of Molecular Science and Technology, National Taiwan University (NTU-MST), Taipei 10617, Taiwan
[b] Molecular Science and Technology Program, Taiwan International Graduate Program (TIGP), Academia Sinica, Taipei 11529, Taiwan.
[c] Center for Condensed Matter Sciences, National Taiwan University, Taipei 10617, Taiwan. E-mail: qorbani@ntnu.edu.tw; chenkh@pub.iams.sinica.edu.tw; chenlc@ntu.edu.tw
[d] Center of Atomic Initiative for New Materials, National Taiwan University, Taipei, 10617, Taiwan
[e] Department of Mechanical Engineering, National Chin-Yi University of Technology, Taichung 411030, Taiwan.
[f] Sustainable Chemical Science and Technology, Taiwan International Graduate Program, Academia Sinica, Nankang, Taipei 11529, Taiwan
[g] Institute of Chemistry, Academia Sinica, Nankang, Taipei 11529, Taiwan
[h] Department of Applied Chemistry, National Yang Ming Chiao Tung University, Hsinchu, 30010, Taiwan
[i] Institute of Atomic and Molecular Sciences, Academia Sinica, Taipei 10617, Taiwan
[j] Department of Chemistry, National Taiwan University, Taipei 10617, Taiwan
[k] Undergraduate Program of Electro-Optical Engineering, National Taiwan Normal University, Taipei 11677 Taiwan
[l] Institute of Electro-Optical Engineering, National Taiwan Normal University, Taipei 11677, Taiwan
[m] Department of Physics, National Taiwan University, Taipei 10617, Taiwan
Supplementary Information available: [Fig. S1–S19 and Table S1-14]

studies have focused on surface engineering to modify surface atomic structure to enhance the efficiency of PC-CO_2RR.[13, 15-17] For example, Zhou and coworker manipulated charge accumulation by anchoring Au single atoms and regulating the vacancy types in the host material. As a result, CO_2 interaction with the catalyst surface changed from physical to chemical adsorption.[13] Chemisorption of CO_2 on the catalyst surface leads to electron transfer from the catalyst to the anti-bonding orbitals of CO_2, which weakens the C=O bonds and facilitates subsequent chemical transformations.[18] This structural change converts CO_2 to nucleophilic or a nucleophile, leading to easier activation of CO_2 for photocatalytic conversion.[18-20]

To achieve surface charge accumulation, doping engineering is the most effective method.[21-24] However, conventional doping methods, such as one-pot synthesis, may not be ideal since they can alter the entire crystal structure of the catalyst and potentially introduce detrimental defects and cause significant carrier recombination.[25-27] In contrast, the wet impregnation approach enables selective modification of the surface properties by anchoring dopants on the host semiconducting material without affecting its bulk characteristics.[25, 28] Hence, anchored dopants can function as supplementary catalytic active sites directly at the surface–ambient interface.[28-30]

Currently, single-atom catalysts (SACs) have garnered immense interest due to their exceptional ability to significantly boost catalytic performance even with minimal metal loading. Beyond merely enhancing physical properties such as light absorption, charge transfer and separation, and introducing new active sites,[31-32] recent studies have highlighted that these improvements fundamentally stem from the precise control of electronic structures.[33] SACs enable the strategic regulation of orbital electron occupancy in adsorbates, thereby stabilizing specific key intermediates.[34-35] Consequently, research has begun to focus on dual or multi-single-atom systems to steer product selectivity from C1 toward C2 products.[36-37] By manipulating surface charge populations, it is possible to finely tune adsorption strength and intermediate stability, which is a vital consideration for the future development of multi-carbon fuels.

However, a significant challenge remains: the selection of the optimal transition metal atom for anchoring lacks a systematic, predictable guideline. Existing studies often rely on trial-and-error, limiting the efficient rational design of advanced catalysts. This limitation is particularly evident in the sparse exploration of spin effects on the occupancy of antibonding orbitals within key intermediates. Such electronic regulation is essential for optimizing the electronic acceptance-donation interaction between the catalyst and reactants, as recent studies suggest that spin-polarized states can significantly stabilize intermediate species through d-orbital rearrangement.[34-35] Addressing this crucial gap, our study establishes a clear selection mechanism. We propose that the key to maximizing electron enrichment on the model catalyst surface lies in the synergistic effect of the number of metal's valence electron and its electronegativity. This principle allows us to predictively select single transition metal atoms that can induce the strongest localized charge accumulation, optimizing CO_2 activation. Ultimately, electronegativity and valence electron count can serve as robust descriptors to predict and guide the selection of suitable transition metals, thereby laying a foundational framework for the rational design of high-performance catalytic materials.

Inspired by the above statements, we designed a series of transition metal-anchored WO_3 catalysts to enhance CO_2 adsorption and promote CO_2 reduction. Notably, WO_3 nanoplates is selected as the model catalyst due to its earth-abundancy, economic cost, nontoxicity, and photostability.[38-39] The wet impregnation method was employed to selectively introduce the fourth period transition metals (Cr, Fe, and Ni) as anchoring dopants on the surface of WO_3. These elements were selected due to their excellent catalytic performance and their capability to effectively modulate surface charge density.[21, 40-41] Characterization techniques, including X-ray absorption near-edge structure (XANES), X-ray photoelectron spectroscopy (XPS), in situ Fourier transform infrared spectroscopy (FTIR) spectroscopy, and density functional theory (DFT) calculations, revealed modulation of charge density distribution and *COOH key intermediate stabilization, asterisks stand for the active site, when transition metals are anchored on the surface. The enhancements of CO_2 adsorption and activation were also proved through the theoretical calculations and experimental PC-CO_2RR. Ultimately, a strong correlation between charge accumulation, CO_2 adsorption, and activation was observed, providing valuable insights for the design of next-generation catalysts.

Experiment

2.1 Chemicals

All chemicals and reagents were of analytical grade and used directly without further purification. Tungsten(VI) chloride (WCl_6, ≥ 99.9%) was purchased from Sigma-Aldrich. Oxalic acid ($H_2C_2O_4$, anhydrous, 98%) was purchased from Alfa-Aescar. Chromium (III) nitrate nonahydrate ($Cr(NO_3)_3{\cdot}9H_2O$, 99%), iron (III) nitrate nonahydrate ($Fe(NO_3)_3{\cdot}6H_2O$, 99%), and nickel nitrate hexahydrate $Ni(NO_3)_2{\cdot}6H_2O$, 99%) were obtained from Sigma-Aldrich. Ethyl alcohol (99.5%) was bought from Shimakyu's Pure Chemicals (Osaka, Japan).

2.2 Preparation of Catalysts

2.2.1 Synthesis of WO_3

WO_3 was prepared via the solvothermal method, following literature report.[42] First, 0.4 g WCl_6 was dissolved in 80 ml of ethanol. Subsequently, 4 g of oxalic acid was added to the solution, and stirring was continued until the solution changed to transparent color. Then, the solution was transferred to a sealed 100 mL Teflon-lined stainless-steel autoclave and placed in the oven at 100 °C for 24 h. After the heating process, the autoclave was cooled naturally to room temperature. The WO_3 powders were then collected by centrifugation and washed three times with deionized (DI) water and absolute ethanol. Subsequently, the collected products were subjected to freeze-drying to prevent particle aggregation. Finally, the products were annealed at 165 °C under atmosphere conditions to enhance the crystallinity.

2.2.2 Synthesis of SA-M/WO_3 (M = Cr, Fe, Ni)

SA-M/WO_3 denotes single atom anchoring on WO_3, where M represents the transition metals that are anchored onto the WO_3 surface. SA-Fe/WO_3 was synthesized using the wet impregnation method.[43-44] Initially, 1 mmol of $Fe(NO_3)_3{\cdot}9H_2O$ and 20 ml of ethanol were added to a flask. The solution was then bubbled with high-purity argon for 30 minutes to remove any dissolved gas. Then, 80 mg of WO_3 powder was added to the solution and stirred to evenly disperse the powder. The solution was heated to 80 °C using an oil bath to facilitate the anchoring of Fe ions onto the surface of WO_3. For SA-Cr/WO_3 and SA-Ni/WO_3, the procedures were the same, with

View Article Online
DOI: 10.1039/D5TA10187E

only the metal precursors changed to $Cr(NO_3)_3{\cdot}9H_2O$ and $Ni(NO_3)_2{\cdot}6H_2O$, respectively.

2.3 Material Characterization

The crystal structure of the catalysts was analyzed using a powder X-ray diffractometer (XRD, Bruker, D2 Phaser) with Cu K_α radiation (λ = 0.1540 nm). The catalyst morphologies were studied using scanning electron microscopy (SEM, JEOL, JSM-6500), high-resolution transmission electron microscopy (HRTEM, EOL JEM-2100F), and scanning transmission electron microscopy (STEM, JEOL, JEM-ARM300F2), operated at 200 kV. Surface area of catalysts were studied by Brunauer–Emmett–Teller analysis (BET, BELSORB MAX II). CO_2 adsorption behavior was conducted using temperature-programmed desorption (TPD) measurements (AutoChem II 2920 Micrometrics). Light absorption measurement was performed by ultraviolet-visible-near infrared spectroscopy (UV-Vis-NIR, JASCO, V-670) with an integrated sphere using $BaSO_4$ powder as the standard reference. Photoluminescence (PL) spectra were measured using a custom-built confocal fiber-microscope integrated with a HORIBA iHR550 system, equipped with a Syncerity BI-NIR CCD camera (wavelength range: 400 to 1075 nm) and a diode laser (405 nm) as the excitation source. Time-resolved photoluminescence (TRPL) signals were collected using a photomultiplier detector (PicoQuant, PMA192, wavelength range: 230 to 920 nm). XPS was measured by an X-ray photoelectron spectroscopy system (ULVAC-PHI, PHI 5000 VersaProbe III) using monochromated Al Kα (1486.6 eV) X-ray as the excitation source. The XPS signals were calibrated by C 1*s* at 284.6 eV. Element composition was measured by inductively coupled plasma optical emission spectroscopy (ICP-OES, Agilent 710-ES). X-ray absorption spectroscopy (XAS) spectra were acquired in National Synchrotron Radiation Research Center (NSRRC, Hsinchu, Taiwan). W L_3 edge was performed under transmission mode in NSRRC TLS BL01 C1. Cr *K*-edge, Fe *K*-edge and Ni *K*-edge were collected under fluorescence mode in NSRRC TPS BL44 A. Reaction intermediates formed during the photoreduction process were monitored using in-situ FTIR spectroscopy (Bruker Tensor 27).[23, 45-46]

2.4 Photocatalytic CO2 Reduction Reaction

A batch-type photocatalytic CO_2 reduction experiment was conducted to investigate the performance of the photocatalyst. Prior to the photocatalytic CO_2 reduction test, 50 mg of photocatalyst was placed in a homemade gas-tight quartz reactor with a 30-mL volume and evacuated to remove any air. The reactor was then filled with high-purity CO_2 (99.9999%), which passed through a water bubbler at a constant flow rate of 100 sccm for 30 minutes under atmospheric pressure. A 150 W AM1.5 solar simulator (Xe lamp) with an intensity of 100 mW cm^{-2} was used as the light source. After 4 h of light exposure, the photocatalytic products were analyzed by gas chromatography (GC; HP 6890 GC-HID) using a Shin-Carbon ST column for product separation. For the isotope test, $^{12}CO_2$ was replaced by $^{13}CO_2$, and the light exposure time was extended to 24 h. The photocatalytic products were analyzed by mass spectrometry (Agilent 7890 CB). The apparent quantum efficiency (AQE) is defined by the ratio of the effective electrons utilized in solar fuel production to the total incident photons on the catalyst. AQE was calculated using the following equation:

$$AQE(\%) = \frac{\text{number of electrons}}{\text{total photons incident on catalyst}} \times 100\% = \frac{\alpha \times Y \times N}{\theta \times T \times S} \times 100\%, \quad (1)$$

where α represents the number of electrons involved in solar fuel formation (α_{CO} = 2, α_{CH_4} = 8, and α_{H_2} = 2), Y is yield of solar fuel products, N is Avogadro's number, θ is the photon flux, T is the irradiation time, and S is the irradiation area. For absorbed photon quantum efficiency ($APQE$), the total incident photons on the catalyst are replaced by the total photons absorbed ($\lambda < \lambda_g$) by the catalyst. In the case of SA-Fe-WO_3, N = 6.022×10^{23} mol^{-1}, θ = 2.58×10^{17} s^{-1} cm^{-2} (integration photons from 300–1100 nm), T = 4 h, S = 4 cm^2. For $APQE$ calculation, θ ($\lambda < \lambda_g$) = 8.86×10^{15} s^{-1} cm^{-2} (λ_g = 413 nm).

2.5 Theoretical Calculations.

Spin-polarized DFT calculations were performed by the Vienna Ab initio Simulation Package (VASP).[47] The projector augmented-wave (PAW) method was employed to describe core-valence interactions.[48] The exchange-correlation functional was treated within the generalized gradient approximation (GGA) using the Perdew–Burke–Ernzerhof (PBE) scheme.[49] A 2×2×4 supercell of WO_3 (cubic phase, space group $Pm\bar{3}m$) was constructed as the computational model. The plane-wave cutoff energy was set to 600 eV for all models. Valence electron configurations are $5d^5 6s^1$ for W, $2s^2 2p^4$ for O, $3d^5 4s^1$ for Cr, $3d^7 4s^1$ for Fe, and $3d^9 4s^1$ for Ni. A k-point convergence test was performed, leading to the selection of a 4×4×1 k-point mesh, as shown in Fig. S1. Electronic and ionic relaxations were carried out with convergence criteria of 10^{-5} eV for energy and 0.005 eV $Å^{-1}$ for forces, respectively. To eliminate the interaction between periodic images, a vacuum space (> 20 Å) was added in the z-direction.

The formation energy (ΔE_f) is calculated as:

$$\Delta E_f = E(\text{anchored } WO_3) - E(WO_3) - \sum_i n_i \mu_i, \quad (2)$$

Where $E(\text{anchored } WO_3)$ and $E(WO_3)$ represent the electronic energies of the WO_3 supercell with and without the metal dopant, respectively. n_i denotes the number of atoms added (n_i > 0) or removed (n_i < 0) relative to the WO_3 supercell, and μ_i is the chemical potential of the atom i, obtained from its pure metal phase. CO_2 adsorption energy was calculated by taking the electronic energy of the system with CO_2 adsorbed and subtracting the combined electronic energy of the pristine surface and the energy of an isolated CO_2 molecule.

The Gibbs free energy was calculated by adding thermal corrections to the electronic energy, as shown in equation (3)[12, 50-52]:

$$G = E_{DFT} + ZPE + H_{(0\to T)} - TS \quad (3)$$

Where E_{DFT} is the electronic energy. ZPE, $H_{(0\to T)}$, and S represent the zero-point energy, enthalpy contribution, and entropy,

View Article Online
DOI: 10.1039/D5TA10187F

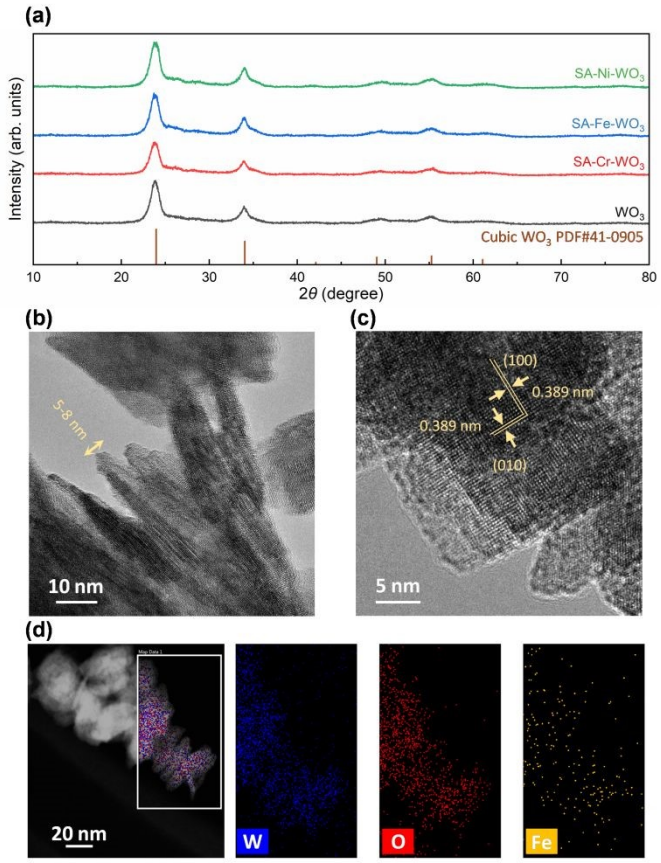

Fig. 1 Material characterizations. (a) XRD patterns of WO_3, SA-Cr-WO_3, SA-Fe-WO_3, and SA-Ni-WO_3. (b, c) HRTEM images of SA-Fe-WO_3 with different magnifications. (d) HAADF and EDS elemental mapping images of SA-Fe-WO_3.

respectively, obtained from vibrational frequency calculations. Only the vibrations of the active sites and adsorbates were considered, while the remaining catalyst atoms were assumed negligible and fixed at their optimized positions. T denotes the temperature, which was set to 300 K in all calculations. In the reaction pathway diagram, the free energy changes (ΔG) of intermediates are referenced to the free energies of a gas-phase CO_2 molecule, the clean surface, and half the free energy of an H_2 molecule multiplied by the number of added hydrogen atoms.[12]

Results and discussion

To investigate the impact of surface atomic structure and electron density distribution on PC-CO_2RR, wet impregnation methods were employed to anchor the desired transition metals onto the surface of WO_3. This method enables modification of the WO_3 surface while maintaining its crystalline structure and preserving its bulk properties. Hence, it hinders the PC-CO_2RR performance from being affected by other factors.

Firstly, XRD patterns and TEM analyses were conducted to confirm the crystal structure of as-synthesized WO_3 and SA-M-WO_3 (M = Cr, Fe and Ni). As depicted in Fig. 1 (a), the XRD patterns reveal that all the diffraction peaks of the as-synthesized WO_3 are consistent with the cubic phase WO_3. The TEM images illustrate a cubic nanoplate morphology for WO_3 with average diameters of 50 nm and thicknesses ranging from 5 to 8 nm, which is beneficial for interlayer charge transfer (Fig. 1 (b-c)). After wet impregnation process, the XRD patterns of SA-Cr-WO_3, SA-Fe-WO_3, and SA-Ni-WO_3 are nearly identical to those of as-synthesized WO_3. This indicates that no metal or metal oxide clusters were formed, and no metals were intercalated during surface modification process. TEM and SEM images (Fig. S2 and S3) show no significant morphological changes. To evaluate surface area variations, BET analysis was performed, revealing similar surface areas across all samples (Fig. S4). The results exhibit a typical Type II isotherm curve with a Type H3 hysteresis loop,

characteristic of plate-like particle aggregation.[53] Additionally, UV-Vis measurements were conducted to confirm light absorption properties, showing an absorption edge near 450 nm in all samples (Fig. S5).[54] Power-dependent PL analysis were also carried out to examine the light emission properties (Fig. S6). The results showed that intensity ratio of emission peak E_A and E_B under different excitation power (0.25 to 15.25 mW) is similar, implying all the modified samples have optical properties similar to the pristine WO_3. Based on above observations, it can be concluded that that the surface modification introduces new catalytic active sites without affecting the electronic structure, accessible surface area, or morphology. To confirm the presence of anchored metals and their distributions, HRTEM, high-angle annular dark-field STEM, and energy-dispersive X-ray spectroscopy (EDS) elemental mapping images were recorded. As shown in Fig. 1 (c), the interplanar spacing

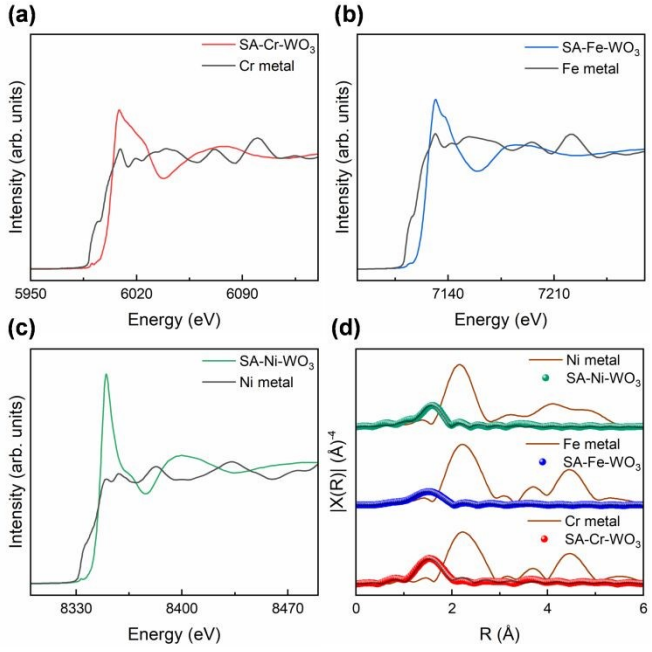

Fig. 2 Structural characterization of transition metal-anchored WO_3 by XAS. XANES spectra (fluorescence mode) of (a) SA-Cr-WO_3, (b) SA-Fe-WO_3, and (c) SA-Ni-WO_3. (d) FT-EXAFS fitting results of transition metal-anchored WO_3. The black line represents the fitting curve, while the brown line represents the standard metal reference.

View Article Online
DOI: 10.1039/D5TA01875E

of SA-Fe-WO_3 nanoplates is 3.9 Å corresponding to (100) and (010) planes of cubic WO_3.[55-56] The observation of these mutually perpendicular lattice planes within the nanoplate confirms that the primary exposed surface (the basal plane) is the (001) facet. No additional metals or metal oxides were observed in the HRTEM images. Meanwhile, EDS elemental mapping images show that W, O and Fe are uniformly distributed (Fig. 1 (d)), confirming the atomically dispersed Fe on the WO_3 nanoplates. We observed the same for SA-Cr-WO_3 and SA-Ni-WO_3 (Fig. S7). Additionally, ICP-OES was performed to precisely determine the elemental composition of the materials (Table S1). The results indicate that the metal doping levels (*i.e.*, M/(W+O)) are approximately 1% for all samples.

To identify the chemical information and coordination environment of loaded metals (Cr, Fe and Ni) in the SA-M-WO_3 samples, XAS was employed to measure the *K*-edge of Cr, Fe and Ni, respectively (Fig. 2 (a–c)). X-ray absorption near-edge spectroscopy (XANES) spectra of all the Cr, Fe, and Ni *K*-edge exhibit noticeably different spectral curves in contrast to the standard metal foil reference. The white line edge shows the much stronger intensity for the *K*-edge of the Cr, Fe, and Ni spectrum, indicating the loaded metals are in the oxidized state rather than the metallic state, implying no metal cluster on the surface. However, their XANES spectra also slightly deviated from their typical metal oxide spectrum. To further confirm the exact coordination environment of loaded metal, the Fourier transform of the Cr, Fe and Ni *K*-edge k^3-weightede extended X-ray absorption fine structure (EXFAS) were processed to acquire bond length information in real (R) space. As shown in Fig. 2 (d), EXAFS spectra of SA-Cr-WO_3, SA-Fe-WO_3 and SA-Ni-WO_3 exhibit the main peaks at 1.51, 1.52 and 1.57 Å, respectively, which are close to the first shell of M–O bond length.[57-59] EXAFS fittings were also processed with the model of metal anchored in bond with oxygen, which agree well with the experimental results. The details of EXAFS fitting parameters are shown in Table S2. Moreover, no other extra peaks were found in the range of 2 to 4 Å, representing there are no M–M bond or second shell of M–O–M bond were formed. It provides the evidence that loaded metals are atomically dispersed and isolated bonded on WO_3 surface.

XPS spectra were recorded to investigate the interaction between the loaded metals and WO_3, chemical compositions, and insights into the charge transfer behavior. Firstly, the core level spectra of loaded metals were measured to confirm their successful incorporation onto the WO_3 surface (Fig. S8). The peak positions of these metals correspond to their oxide states, indicating bonding with surface oxygen, which is consistent with the XAS results. To further examine charge transfer behavior, the core levels of tungsten and oxygen were analyzed. As depicted in Fig. 3 (a), the doublet peaks of W 4*f* in pristine WO_3 were observed at 37.5 eV (W $4f_{5/2}$) and

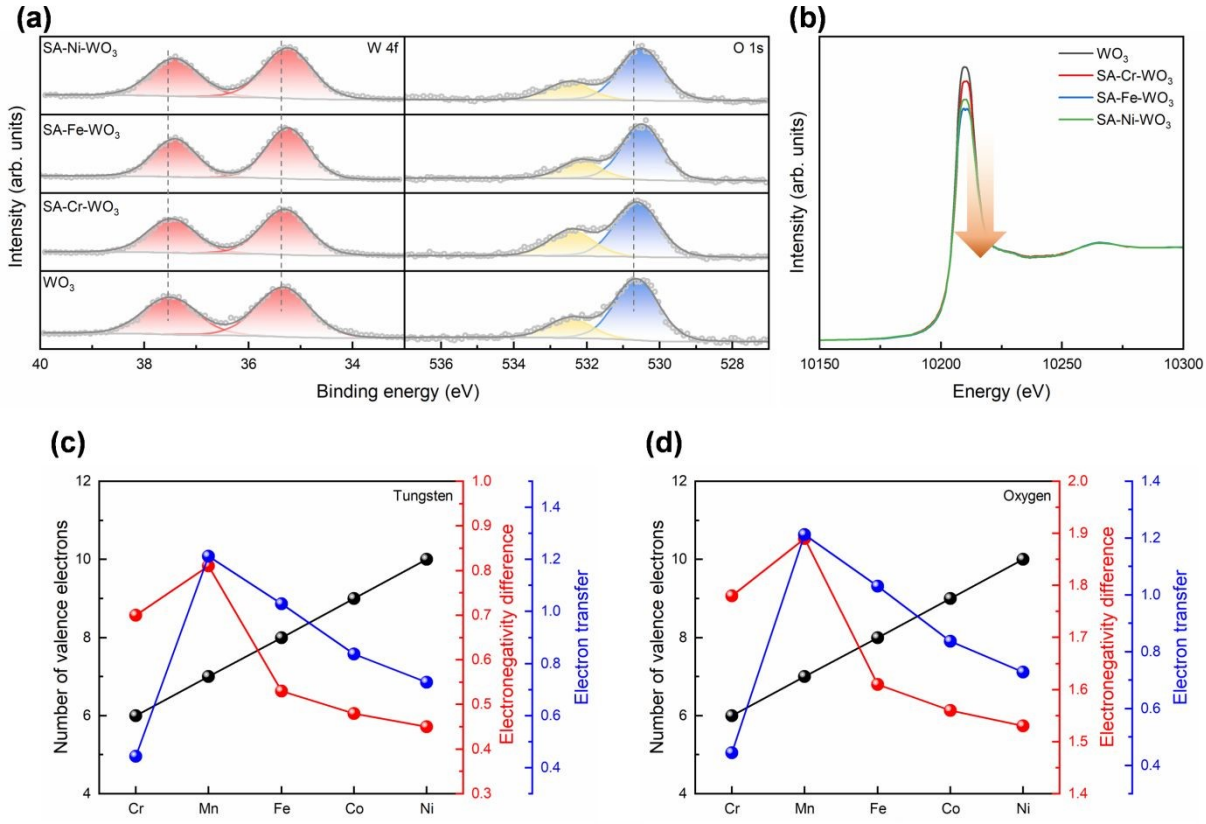

Fig. 3 Charge transfer analysis with different metal (Cr, Fe, and Ni) modifications. (a) W 4*f* and O 1*s* spectra of WO_3, SA-Cr-WO_3, SA-Fe-WO_3, and SA-Ni-WO_3. (b) XANES spectra (transmission mode) at the W L_3-edge for WO_3, Cr-WO_3, Fe-WO_3, and Ni-WO_3. (c, d) Relationship of charge transfer, valence electrons and electronegativity of W and O elements respectively. (Electron transfer is calculated from DFT.)

View Article Online
DOI: 10.1039/D5TA10187F

35.3 eV (W 4$f_{7/2}$). For O 1*s* spectra, pristine WO_3 also exhibits two peaks located at 530.7 eV and 532.5 eV, which are attributed to lattice oxygen and -OH, respectively.[60] It should be noted that the ratio between O–to–W matches with the stoichiometric ratio (Table S3). After metal loading, both W 4*f* and O1*s* peaks shifted toward lower binding energy, indicating electron transfer from the loaded metals to WO_3. The shift in XPS signals followed the trend: SA-Fe-WO_3 > SA-Ni-WO_3 > SA-SA-Cr-WO_3 > WO_3, exhibiting a volcano plot behavior. Particularly, SA-Fe/WO_3 exhibited the most significant shift for W 4*f* from 35.3 to 35.2 eV and for O 1*s* from 530.7 to 530.5 eV, implying the strongest interaction between Fe atoms and WO_3, with more electrons transfer from Fe atoms to WO_3. Notably, O 1*s* displays a larger change since it is in the first shell of the doped metals. In addition, XAS measurements were also conducted to elucidate the charge transfer behavior within the materials. The intensity of the white line in the *L*-edge spectra is an indicator of *d*-orbital occupancy, *i.e.*, the lower edge intensity indicates higher *d*-orbital occupancy. The normalized W L_3 edge spectra are presented in Fig. 3 (b). It can be observed that the intensity of the W L_3 edge decreases while the metals are loaded onto the WO_3, indicating a decrease of empty orbitals. It implies that introducing metals has led to charge transfer between loaded metals and WO_3. While the loaded metals provide the excess electrons to fill the *d*-orbitals, the excited electrons are not allowed to process bound state transition (2*p* to 5*d*). Among all the samples, it was observed that SA-Fe-WO_3 exhibited the greatest decrease, indicating that the charge density transfer between Fe and WO_3 is the highest, while that between Cr and WO_3 is the lowest. This result is also consistent with the XPS results. Based on the initial material design principles, doped metal atoms with a higher number of valence electrons are more likely to donate electrons to the substrate material. Meanwhile, the electronegativity of element also influences the degree of electron transfer, as shown in Fig. 3 (c–d). Hence, it can be concluded that Fe can be considered as the single atom with the most electron density transfer to WO_3.

To study the impact of different metal loading on the CO_2RR performance, we conducted a series of PC tests. For these tests, the materials were sealed in a batch-type quartz reactor filled with CO_2 and water vapor, followed by light irradiation for 4 h. As shown in Fig. 4 (a), the main products for pristine WO_3 are CO, H_2, and CH_4, with yields of 4.5, 0.97, and 0.2 μmol g^{-1}, respectively. Doping with Cr, Fe, and Ni showed improvements in the product yields. Specifically, with Cr doping, the yields of CO, H_2, and CH_4 increased to 7, 1.3, and 0.7 μmol g^{-1}, respectively. Fe doping resulted in a highest increase in yield among all three samples, with CO, H_2, and CH_4 yields reaching 12.1, 3.1, and 0.6 μmol g^{-1}, respectively, which are approximately three times higher than those of pristine WO_3. However, Ni doping led to a modest increase in yield, with the CO, H_2, and CH_4 production falling to 8.9, 1.9, and 0.6 μmol g^{-1}, respectively. This volcano-like behavior is analogous to the degree of charge transfer observed (Fig. 4 (a)). While the charge transfers within the material increases, the photocatalytic CO_2 reduction activity is also enhanced. This similar trend suggests a correlation between charge transfer and photocatalytic CO_2 reduction activity.

To determine the optimal catalyst configuration, a series of SA-Fe-WO_3 samples with varying Fe concentrations was systematically evaluated. The results indicate that the optimal loading amount is 1.0%, while the CO_2 reduction efficiency begins to decrease as the concentration is further increased to 1.5% (Fig. S9). This performance decline is attributed to the fact that high loading amounts facilitate the formation of metal clusters, which leads to the loss of the unique charge transfer behavior characteristic of isolated single atoms. Supporting this conclusion, XPS results reveal that the 1.5% sample does not exhibit the significant binding energy shifts found at lower loadings, suggesting a lack of effective electronic interaction between the Fe species and the WO_3 support (Fig. S10).

To test the stability of the material under PC-CO_2RR experiment, the samples were recycled after each cycle of photocatalytic CO_2 reduction and then subjected to the same PC test. The results indicate that the samples maintained good stability after five cycles (~20 h). In addition, a blank test experiment was also conducted to

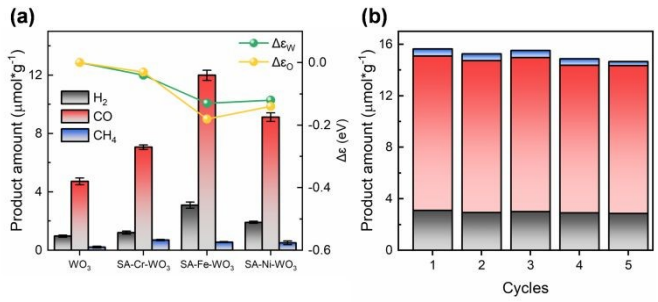

Fig. 4 Photocatalytic CO_2 reduction. (a) Average product yield of WO_3, SA-Cr-WO_3, SA-Fe-WO_3, and SA-Ni-WO_3 for an irradiation time of 4 h. W 4*f* and O 1*s* peak shifts from the XPS results are also included for the comparison. (b) Cycling stability test for SA-Fe-WO_3.

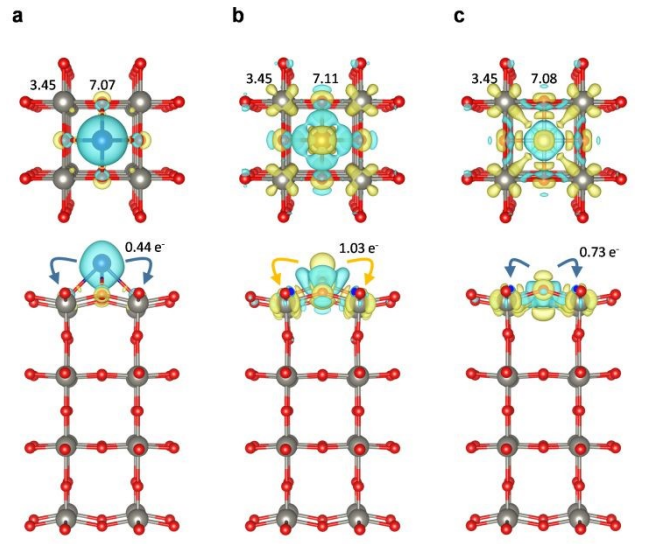

Fig. 5 Charge density distribution analysis. Charge density distribution analysis of (a) SA-Cr-WO_3, (b) SA-Fe-WO_3 and (c) SA-Ni-WO_3. Charge densities with interface values of 0.003 e^- $Bohr^{-3}$. Yellow and cyan areas denote electron accumulation and depletion, respectively. Top: top view. Bottom: side view.

View Article Online
DOI: 10.1039/D5TA10187F

confirm that the CO_2RR products were indeed converted from the CO_2 and not from surface contamination (Fig. S11). Isotope tracer analyses were also performed to understand the carbon source of product CO and CH_4 (Fig. S12). The overall AQE and $APQE$ reached approximately 0.007% and 0.21% which is in the range of highest productivity plants that have typical efficiency of about 1% annually, respectively.[61]

Superior CO_2RR performance is often accompanied with electron localization in material, which is benefit to the CO_2 adsorption and activation.[13, 15-16] Our results show a potential correlation between the charge transfer and CO_2RR activity. To address it in details, we performed DFT calculations to investigate the impacts of anchored Cr, Mn, Fe, Co and Ni atoms on the re-distribution of surface charge density and CO_2 adsorption over WO_3 surface. According to the XRD and TEM results, the cubic WO_3 surface was cleaved along the (001) direction of bulk WO_3. A 2×2×4 supercell was then constructed as the computational model. Based on the XAS results, the doped metal coordinates with oxygen atoms, suggesting two possible anchoring configurations for Cr, Fe, and Ni: (I) Metal is positioned directly on an oxygen site ("M on O") or (II) Metal is surrounded by four oxygen atoms ("M anchored"). Formation energy calculations (Fig. S13) indicate that Cr, Fe, and Ni preferentially adopt the configuration anchored between four oxygen atoms (Fig. S14). The charge density differences were calculated to explore re-distribution of charge density of WO_3 surface. As displayed in Fig. 5, it can be observed that electron accumulation occurs near the W and O atoms adjacent to the doped metals, *i.e.*, surface charge density re-distributed or creating localized electron-rich regions, while electron depletion occurs at the doped metals. To further quantify the amount of the transferred electron from the anchoring metals, Bader charge analysis was conducted.[62] The results clearly show that anchoring Cr, Mn, Fe, Co and Ni can transfer 0.44, 1.21, 1.03, 0.84 and 0.73 e^- to the neighboring atoms, respectively, thereby enhancing the surface electron density. Specifically, the electron population of the neighboring W atoms increases from 3.45 e^- in pristine WO_3 to 3.47, 3.59, 3.58, 3.53 and 3.52 e^- for SA-Cr, SA-Mn, SA-Fe, SA-Co and SA-Ni, respectively. A similar trend is observed for the neighboring O atoms, where the electron population rises from 6.99 to 7.07, 7.14, 7.10, 7.11, and 7.08 e^-. This quantitative trend, summarized in Fig. S15 and Table S4, aligns perfectly with our XPS and XANES findings. The charge localization induced by Fe can be attributed to the ideal balance between its valence electron count and electronegativity (see Fig. 3 (c–d)). While Cr has a relatively low electronegativity, its limited number of valence electrons ($3d^54s^1$) restricts the total amount of transferable charge. Conversely, although Ni possesses the highest valence electron count ($3d^94s^1$), its high electronegativity exerts a stronger pull on its electrons, thereby hindering effective transfer to the WO_3 substrate. Mn ($3d^54s^2$) and Fe ($3d^74s^1$) represents a synergistic optimum, providing a sufficient valence electron supply while maintaining a moderate electronegativity, which maximizes the localized surface charge density to promote CO_2 activation.

In addition, the next question would be "how does the position of the metal dopant influence charge density distribution?". To address this question, we calculated the charge density distribution with metals placed in various positions, as illustrated in Fig. S15. The results reveal minimal charge transfers when the metal substitutes W sites. Furthermore, when the dopants occupy interstitial sites within the WO_3 lattice, the surface W atoms exhibit a tendency to lose electrons. It represents that surface convert to electron deficiency condition. This suggests that only when metals are anchored on the WO_3 surface can effectively induce charge

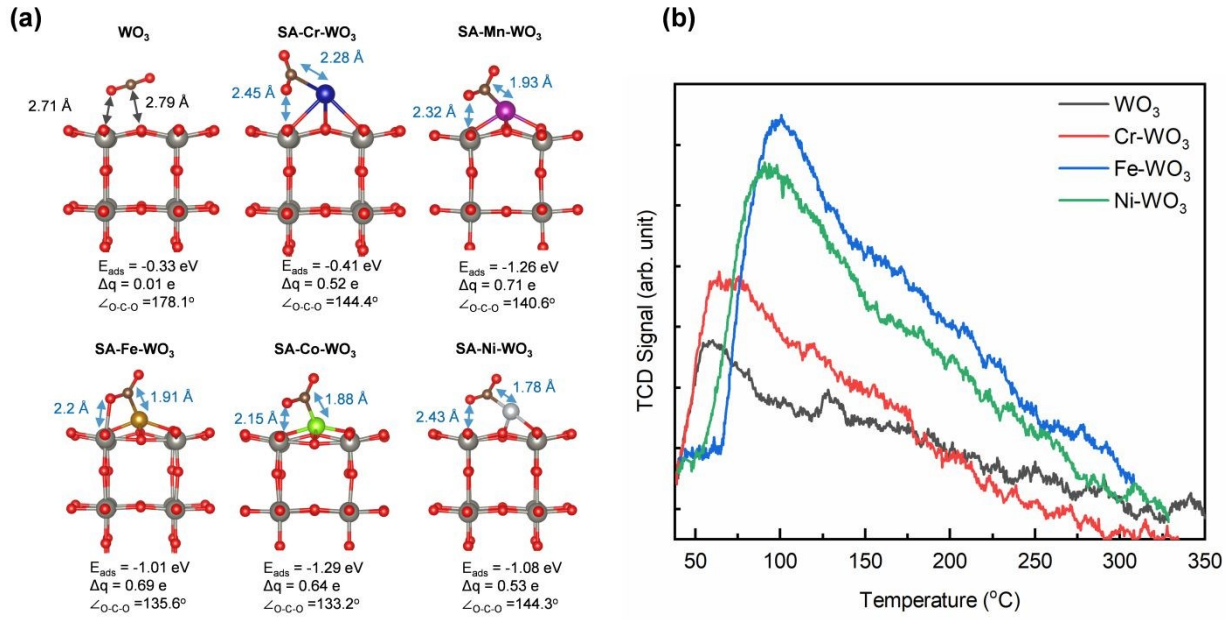

Fig. 6 CO_2 adsorption model and desorption behavior. (a) CO_2 adsorption models on WO_3, SA-Cr-WO_3, SA-Mn-WO_3, SA-Fe-WO_3, SA-Co-WO_3 and SA-Ni-WO_3. (b) CO_2-TPD profiles of transition metal-anchored WO_3.

View Article Online
DOI: 10.1039/D5TA10187F

accumulation on the catalyst surface. However, substitutional and interstitial site doping are thermodynamically more stable than anchored doping, as shown in Fig. S16. Therefore, to promote metal anchoring on the catalyst surface and enhance kinetic feasibility, we employed a wet impregnation approach instead of in-situ doping methods. Furthermore, considering that XPS analysis revealed the presence of surface hydroxyl groups (-OH), we constructed hydroxylated surface models (OH-WO_3 and SA-Fe-OH-WO_3) to evaluate the impact of -OH groups on the electronic environment. As summarized in Table S5, the introduction of surface -OH groups do not significantly alter the charge density of the surrounding W and O atoms. The consistent charge distribution between the pristine and hydroxylated surfaces confirms that the predictive selection principle remains robust under realistic, hydrated reaction conditions.

To elucidate the role of anchoring metals in modulating CO_2 adsorption, we constructed CO_2 adsorption models to calculate both the adsorption energy and the associated charge transfer. Initially, several possible adsorption structures were optimized to identify the most stable CO_2 adsorption configurations. Their adsorption model and adsorption energy are shown in Fig. S17. The most stable configurations for CO_2 adsorbed on WO_3, SA-Cr-WO_3, SA-Mn-WO_3, SA-Fe-WO_3, SA-Co-WO_3, and SA-Ni-WO_3 are displayed in Fig. 6 (a). The results indicate that CO_2 molecules can spontaneously adsorb onto all systems, as evidenced by negative adsorption energies. The transition metal anchored samples exhibit stronger CO_2 adsorption compared to the pristine WO_3, as reflected by their more negative adsorption energies. The adsorption energy of CO_2 basically follows the trend of charge transfer: SA-Co-WO_3 ≈ SA-Mn-WO_3 > SA-Fe-WO_3 ≈ SA-Ni-WO_3 > SA-Cr-WO_3 > WO_3, suggesting that increased localization of electrons enhances CO_2 adsorption. Specifically, CO_2 exhibits weaker interactions on pristine WO_3, with an adsorption energy of −0.33 eV, while SA-Cr-WO_3, SA-Mn-WO_3, SA-Fe-WO_3, SA-Co-WO_3 and SA-Ni-WO_3 show stronger interactions (mixed configuration) with adsorption energies of −0.41, −1.26, −1.01, −1.29 and −1.08 eV, respectively. In addition, SA-Fe-WO_3 exist another chemisorption mode of CO_2 (oxygen-down configuration) with adsorption energy of -0.48 eV. Therefore, it can be expected that SA-Fe-WO_3 system can have higher possibility to adsorbed the CO_2 for

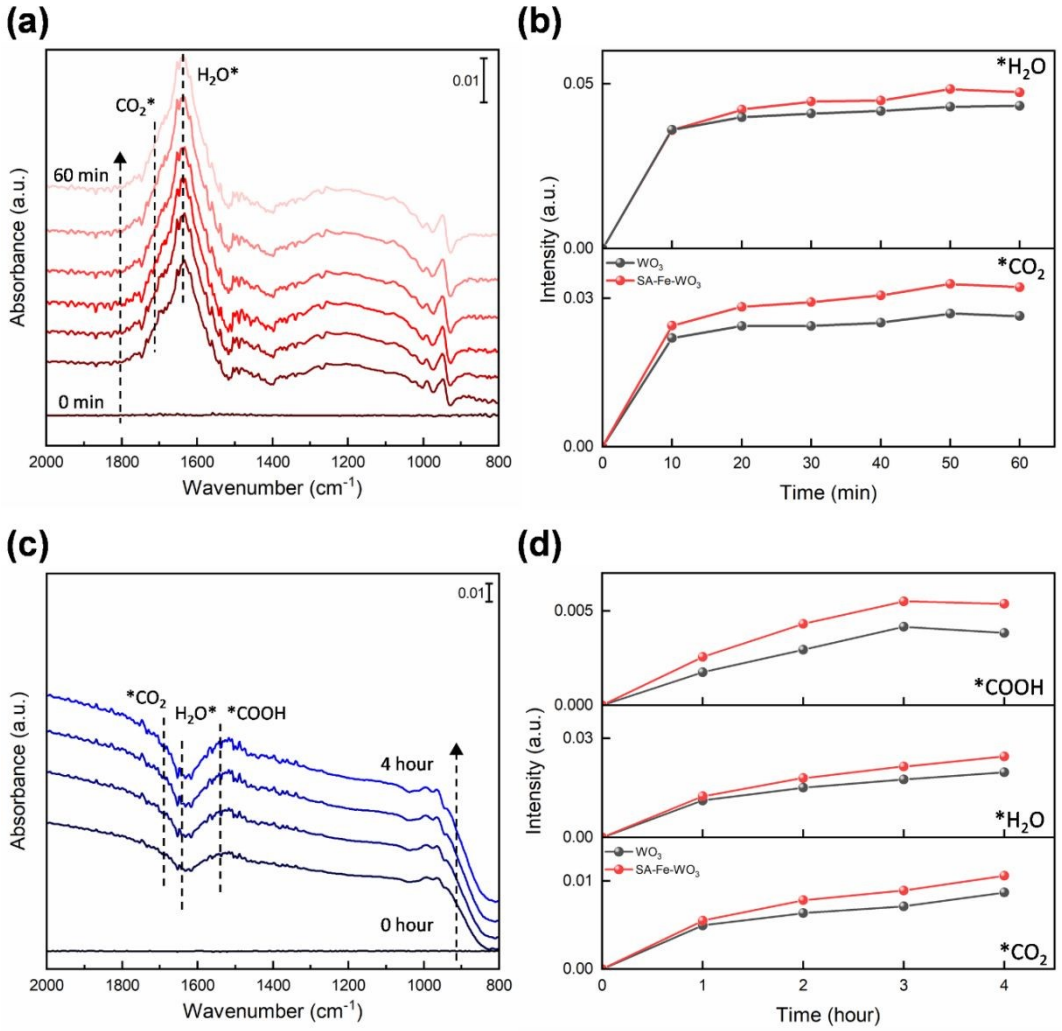

Fig. 7 In-situ FTIR measurements. (a) In-situ FTIR spectra of SA-Fe-WO_3 and (b) variation of IR peak intensities associated with *CO_2 and H_2O*, recorded in CO_2 and H_2O atmospheres under dark conditions. (c) In-situ FTIR spectra of SA-Fe- WO_3 and (d) time-dependent variation of IR peak intensities associated with *CO_2, H_2O*, and the *COOH intermediate, recorded in H_2O and CO_2 atmospheres under light irradiation

View Article Online
DOI: 10.1039/D5TA10187F

activation. Additionally, the configuration of adsorbed CO_2 serves as a crucial descriptor for high-performance catalysts, as the bond length and angle of the CO_2 molecule reflect its activation state.[63] In the pristine WO_3 system, CO_2 preferentially adsorbs on W and O sites, forming O–W and C–O bonds. However, the charge transfer from WO_3 to the CO_2 molecule is merely 0.01 electrons, and the CO_2 molecule remains in a nearly linear configuration (178.1°), characteristic of weak physical adsorption. In contrast, in SA-Cr-WO_3, SA-Mn-WO_3, SA-Fe-WO_3, SA-Co-WO_3 and SA-Ni-WO_3 systems, CO_2 preferentially coordinates with W and the anchored metal sites, forming O–W and C–M bonds, which induce CO_2 bending. The charge transfer from SA-Cr-WO_3, SA-Mn-WO_3, SA-Fe-WO_3, SA-Co-WO_3 and SA-Ni-WO_3 to the CO_2 molecule increases significantly, reaching 0.52, 0.71, 0.69, 0.64 and 0.53 electrons, respectively. Notably, in the oxygen-down configuration of SA-Fe-WO_3, charge transfer can reach up to 0.74 eV. As a result, the C=O bond length elongates from 1.18 Å to 1.26 Å, and the CO_2 molecular angle (∠O–C–O) reduces from 180° to 132.1°. More details are presented in Table S6. These results indicate that charge density localization enhances CO_2 adsorption and activation. To account for more realistic reaction conditions, the influence of surface hydroxylation on CO_2 adsorption was also systematically investigated. As summarized in Table S7, the adsorption energy of CO_2 on the OH-WO_3 exhibits only a minor shift from -0.33 eV to -0.40 eV compared to the pristine surface. For the SA-Fe-OH-WO_3 system, although the presence of surface -OH groups leads to a slight decrease in adsorption strength (from -1.01 eV to -0.78 eV), the adsorption energy remains significantly more favorable than that of both pristine and hydroxylated WO_3 supports. These findings confirm that the Fe single-atom sites maintain their superior CO_2 activation capability even in a hydroxylated environment.

Furthermore, we confirmed the enhancement of CO_2 adsorption through TPD measurements. As shown in Fig. 6 (b), the CO_2-TPD profile of the pristine WO_3 system exhibits a desorption peak near 50°C, indicating the presence of physical adsorption. After anchoring Cr, Fe, and Ni, the desorption peaks shift to higher temperatures, withthe SA-Fe-WO_3 system showing a prominent peak near 110 °C. This shift suggests stronger chemisorption of CO_2 due to interactions with the anchored metal and tungsten. Additionally, a significant increase in peak area is observed, which can be attributed to the two kinds of chemisorbed CO_2 species in the SA-Fe-WO_3 system. These experimental findings meet well with our simulation results. These results clearly reveal that anchored metal modulates the surface charge density distribution of WO_3 to promote CO_2 activation.

In-situ FTIR spectroscopy was employed to elucidate the mechanistic pathway of the anchored-metal system in photocatalyticCO_2 reduction. In-situ FTIR spectra showed that several new characteristic peaks appeared after purging CO_2 and H_2O vapor. (Fig. 7 (a), Fig. S18-19). The peak at 1695 cm^{-1} was assigned to the surface-adsorbed CO_2 ($*CO_2$), while the peaks at 1634 and 3421 cm^{-1} were attributed to the surface-adsorbed H_2O (H_2O*).[23, 45-46] These results confirm that the essential reactants for the CO_2RR were successfully adsorbed on the catalyst surface prior to light irradiation. The peak intensities of $*CO_2$ and H_2O* increased during gas purging (Fig. 7 (b)). Upon light irradiation, the intensities of the $*CO_2$ and H_2O* peaks decreased, signifying the consumption of the adsorbed species during the CO_2RR (Fig. 7 (c), Fig. S18-19). This consumption was observed to be time-dependent, as the peak intensities continuously decreased over the irradiation period (Fig. 7 (d)). The decreases in the peak intensities of $*CO_2$ and H_2O* obtained in the SA-Fe-WO_3 sample is 20 and 25 % higher than that obtained in the pristine WO_3, highlighting that the enhanced reactivity of SA-Fe-WO_3 sample could result from Fe anchoring. Notably, a new peak emerged at 1516 cm^{-1} after light irradiation, corresponding to the *COOH intermediate (Fig. 7 (c)).[23, 64-65] As noted in these references, this peak position is consistent with prior studies on metal oxide photocatalysts, where the characteristic bands of *COOH species are typically observed in the 1500–1560 cm^{-1} region. For example, similar intermediate features have been reported at approximately 1536 cm^{-1} on Bi_2WO_6 surfaces.[23] The peak intensity of this intermediate was 40% greater on SA-Fe-WO_3 than on its pristine WO_3, indicating that Fe anchoring enhances the formation of this key intermediate (Fig. 7 (d)). Those observation is consistent with our DFT calculations and TPD results. These results collectively demonstrate that anchoring Fe atoms significantly enhances CO_2 activation and facilitates the subsequent formation of key intermediates in the photocatalytic pathway.

To further elucidate the origin of the enhanced photocatalytic activity in metal-anchored systems, Gibbs free-energy calculations were conducted on the possible reaction pathways, guided by in-situ FTIR observations of key intermediates. The detailed results are summarized in Fig. 8 and Tables S8–S13. Metal anchoring was found to significantly enhance CO_2 adsorption to form $*CO_2$, decreasing $\Delta G(*CO_2)$ from 0.16 eV for pristine WO_3 to 0.05 eV for SA-Cr-WO_3, and to negative values for SA-Fe-WO_3 (–0.53 eV) and SA-Ni-WO_3 (–0.54 eV), indicating a thermodynamically spontaneous process. This can be attributed to the stronger localized charge density introduced by the anchored metals, which effectively promotes CO_2 adsorption. In the subsequent protonation step, the formation of *COOH was identified as the possible rate-determining step (RDS) on pristine WO_3, with a high $\Delta G(*COOH)$ of 1.5 eV. In contrast, all metal-anchored systems rendered *COOH formation exothermic ($\Delta G < 0$), making the reaction thermodynamically favorable. Among them, the Fe-anchored system exhibited the most pronounced effect, with $\Delta G(*COOH) = -1.73$ eV, consistent with the experimentally observed superior photocatalytic activity. SA-Cr-WO_3 and SA-Ni-WO_3 also facilitated COOH* formation, with $\Delta G(*COOH)$ of –0.47 eV and –0.55 eV, respectively. These results highlight that the stronger localized charge density not only enhances CO_2 adsorption but also stabilizes the first hydrogenated CO_2 intermediate. Notably, unlike other systems, SA-Fe-WO_3 spontaneously cleaved the C-OH bond in COOH*, forming *CO and *OH. Compared with the subsequent step of converting *COOH into $*CO + H_2O$, it can be inferred that the ease of *CO formation follows the order SA-Fe-WO_3 > SA-Ni-WO_3 > SA-Cr-WO_3. SA-Ni-WO_3 exhibited a more favorable $\Delta G(*CO + H_2O)$ of –0.83 eV compared with SA-Cr-WO_3 (–0.03 eV), suggesting that the transformation of *COOH to CO is comparatively less favorable on SA-Cr-WO_3. This explains why the CO_2 conversion efficiency of SA-Ni-WO_3 is higher than that of SA-Cr-WO_3.

To further quantify the impact of charge accumulation on

View Article Online
DOI: 10.1039/D5TA10187F

regulating the adsorption of *COOH, both the adsorption energy and the associated charge transfer are calculated and summarized in Table S14. While *COOH adsorption is energetically unfavorable on pristine WO_3 with adsorption energy 0.51 eV, the introduction of single-atom sites dramatically stabilizes the intermediate, with adsorption energy reaching -1.35 eV and -1.32 eV for SA-Cr-WO_3 and SA-Ni-WO_3, respectively. Structural parameters reveal that the O-C-OH bond angle of the adsorbed species on SACs bends significantly to 115°, indicating a high degree of activation from the linear CO_2 geometry. Furthermore, Bader charge analysis confirms a substantial electron transfer to the *COOH moiety, reaching 1.62 electrons and 1.49 electrons for SA-Cr-WO_3 and SA-Ni-WO_3, respectively, which are significantly higher than the 0.47 e- observed for pristine WO_3. This localized electron enrichment at the active site, driven by the

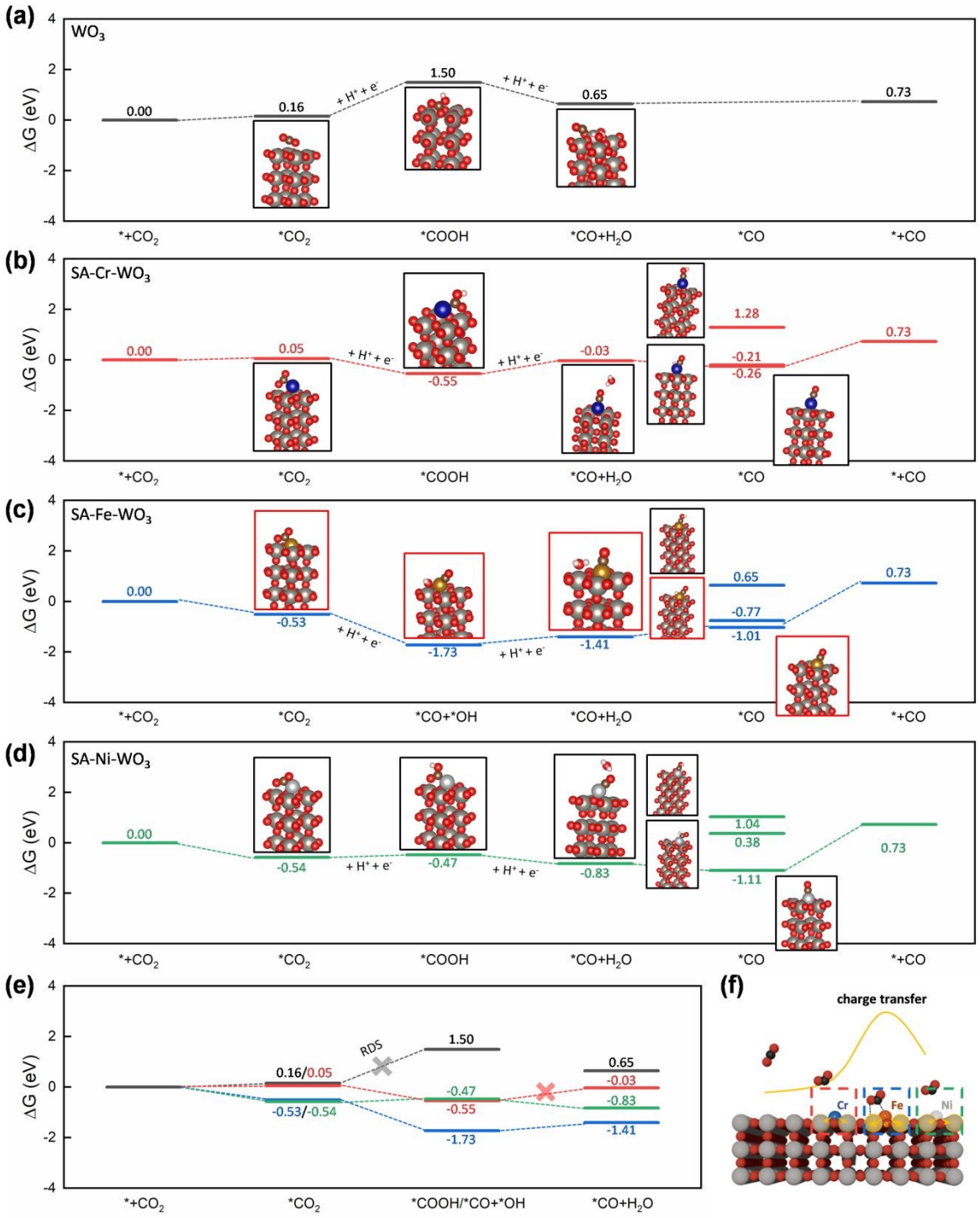

Fig. 8 Gibbs free energy calculation. Free energy diagrams for the photoreduction of CO_2 to CO over (a) pristine WO_3, (b) SA-Cr-WO_3, (c) SA-Fe-WO_3, and (d) SA-Ni-WO_3. (e) Key intermediate states involved in the CO_2-to-CO photoreduction pathway on WO_3, SA-Cr-WO_3, SA-Fe-WO_3, and SA-Ni-WO_3. (f) Schematic of charge transfer over different single atoms and adsorbed CO_2

View Article Online
DOI: 10.1039/D5TA01875

synergistic interaction between the single atom and the WO_3 support, effectively weakens the C-OH bond and promotes the COOH activation.

To further elucidate the prefer product selectivity of CO, *COH and *CHO are aslo processed because both are critical intermediates for CH_4 formation. the Gibbs free energies (ΔG) for the formation of *COH on SA-Cr-WO_3 (1.28 eV), SA-Fe-WO_3 (0.65 eV), and SA-Ni-WO_3 (1.04 eV) are significantly higher than those for *CO formation. Similarly, the ΔG values for the formation of *CHO on SA-Cr-WO_3 (-0.21 eV) and SA-Ni-WO_3 (0.38 eV) are also higher than the energies associated with the *CO species. These elevated energy barriers indicate that the further protonation of adsorbed *CO is thermodynamically unfavorable on the SA-M-WO_3 surfaces. Notably, on the SA-Fe-WO_3 catalyst, the CO-H bond in the potential *CHO intermediates undergoes spontaneous cleavage, which effectively terminates the pathway toward the formation of CH_4. These findings suggest that while the localized charge successfully stabilizes the initial *COOH intermediate, the specific electronic environment of the single-atom sites does not support the subsequent hydrogenation steps required for CH_4 production. Consequently, the catalysts exhibit high selectivity for CO desorption over further reduction because the energy required to reach CH_4 intermediates significantly higher.

The superior performance of SA-Fe-WO_3 is attributed to the maximal electron transfer from Fe to the WO_3 framework, as evidenced by the most significant shifts in XPS binding energies and W L_3-edge XANES intensities. Bader charge analysis confirms that Fe induces the highest localized charge accumulation at neighboring atoms compared to Cr and Ni, which stems from the optimal balance between its valence electron count and electronegativity. This enhanced surface charge localization promotes CO_2 activation and significantly stabilizes the key *COOH intermediate by lowering its formation energy. Collectively, these synergistic electronic factors lower the overall reaction barrier, leading to the observed threefold enhancement in photocatalytic CO_2 reduction efficiency.

Conclusions

In summary, single-atom anchored WO_3 photocatalysts (SA-Cr-WO_3, SA-Fe-WO_3, and SA-Ni-WO_3) were successfully synthesized via the wet impregnation method, with uniform dispersion of metals confirmed by EXAFS analysis. The anchored metals induce a re-distribution of charge density, as supported by experiments (XPS and XAS) and DFT calculations. We observed that anchored metals donate electrons to surrounding atoms, leading to localized charge density accumulation. This resulted in enhanced CO_2 molecule chemisorption, as demonstrated by TPD and DFT analyses. Moreover, Gibbs free-energy calculations and in situ FTIR revealed that *COOH is the key intermediate, and metal anchoring lowers its activation barrier, rendering the reaction thermodynamically spontaneous. Stronger charge-density localization not only enhances CO_2 chemisorption but also promotes CO_2 activation. Consequently, photocatalytic CO_2 reduction reaction performance improved three times with a yield of 12.1 μmol g^{-1} per 4 h (or $APQE$ = 0.21%) for CO product. These findings illustrate a strong correlation between charge density localization, CO_2 adsorption, and CO_2 activation and provide valuable insights for designing improved catalyst surfaces.

Author contributions

C.-Y.H. contributed to the idea, investigation, methodology, experiment, visualization, simulation and writing of the original draft. Y.-R.L. and M.H. assisted the simulation. M.E.A. performed the BET experiments. Y.-F.H. contributed to the conceptualization. T.-Y.L., K. L. and H.-L.W. performed the in-situ FTIR experiments. K.-H.C. and L.-C.C. acquired the funding. M.Q., K.-H.C. and L.-C.C. supervised the project, review and edit the manuscript.

Conflicts of interest

The authors declare no competing financial interest.

Data availability

The data supporting this article have been included as part of the Supplementary Information. Supplementary information: Fig. S1-S19 and Tables S1-S14.

Acknowledgements

This research was financially supported by the National Science and Technology Council (NSTC) in Taiwan under Academic Summit Project (NSTC 112-2639-M-002-005-ASP, NSTC 113-2639-M-002-004-ASP and NSTC 114-2639-M-002-003-ASP), NSTC 111-2112-M-131-002-MY3 and NSTC 111-2112-M-019-006-MY3, as well as the Center of Atomic Initiative for New Materials (AI-Mat), National Taiwan University [111 L9008, 112 L9008, 113 L9008 and 114 L9008], from the Featured Areas Research Center Program within the framework of the Higher Education Sprout Project by the Ministry of Education (MOE) of Taiwan. M.Q. acknowledges support from the National Science and Technology Council (NSTC) Taiwan [grant number: 114-2112-M-003-019-MY2]. In addition, we would like to thank Ms. C.-Y. Chien of Ministry of Science and Technology (National Taiwan University) for the assistance in TEM experiments. Technical support from the Advanced Materials Characterization Lab, Institute of Atomic and Molecular Sciences (IAMS), Academia Sinica, is also gratefully acknowledged. We also acknowledge National Synchrotron Radiation Research Center (NSRRC) TLS 01C1 and TPS 44A for assistance XAS measurement. We are grateful to Computer and Information Networking Center, National Taiwan University for the support of high-performance computing facilities.

References

1. Q. Yi, W. Li, J. Feng and K. Xie, *Chem. Soc. Rev.,* 2015, **44**, 5409-5445.
2. S. Solomon, G.-K. Plattner, R. Knutti and P. Friedlingstein, *PNAS,* 2009, **106**, 1704-1709.
3. J. Fu, K. Jiang, X. Qiu, J. Yu and M. Liu, *Mater. Today,* 2020, **32**, 222-243.

4. M. Aresta, A. Dibenedetto and A. Angelini, *Chem. Rev.,* 2014, **114**, 1709-1742.
5. S. Fang, M. Rahaman, J. Bharti, E. Reisner, M. Robert, G. A. Ozin and Y. H. Hu, *Nat. Rev. Methods Primers,* 2023, **3**, 61.
6. P.-P. Huang, M. Qorbani, Y.-T. Hung, Y.-R. Lai, A. Sabbah, M.-F. Tseng, C.-Y. Huang, S. Koodathil, S. Kholimatussadiah and M. K. Hussien, *ACS Nano,* 2026.
7. Z. Sun, T. Ma, H. Tao, Q. Fan and B. Han, *Chem,* 2017, **3**, 560-587.
8. B. Han, X. Ou, Z. Deng, Y. Song, C. Tian, H. Deng, Y. J. Xu and Z. Lin, *Angew. Chem. Int. Ed.,* 2018, **57**, 16811-16815.
9. W. Yao, B. Wu and Y. Liu, *ACS Nano,* 2020, **14**, 9320-9346.
10. M. Qorbani, A. Sabbah, Y.-R. Lai, S. Kholimatussadiah, S. Quadir, C.-Y. Huang, I. Shown, Y.-F. Huang, M. Hayashi and K.-H. Chen, *Nat. Commun.,* 2022, **13**, 1256.
11. W. Jiang, H. Loh, B. Q. L. Low, H. Zhu, J. Low, J. Z. X. Heng, K. Y. Tang, Z. Li, X. J. Loh and E. Ye, *Appl. Catal., B,* 2023, **321**, 122079.
12. X. Li, Y. Sun, J. Xu, Y. Shao, J. Wu, X. Xu, Y. Pan, H. Ju, J. Zhu and Y. Xie, *Nat. Energy,* 2019, **4**, 690-699.
13. Y. Cao, L. Guo, M. Dan, D. E. Doronkin, C. Han, Z. Rao, Y. Liu, J. Meng, Z. Huang and K. Zheng, *Nat. Commun.,* 2021, **12**, 1675.
14. J. Ji, R. Li, H. Zhang, Y. Duan, Q. Liu, H. Wang and Z. Shen, *Appl. Catal., B,* 2023, **321**, 122020.
15. Y. Wang, C. Ban, J. Meng, J. Ma, H. Zou, Y. Feng, J. Ding, Y. Duan, L. Gan and X. Zhou, *Sep. Purif. Technol.,* 2023, **312**, 123379.
16. H. M. Ngo, U. Pal, Y. S. Kang and K. M. Ok, *ACS Omega,* 2023, **8**, 8876-8884.
17. X. Jiao, X. Li, X. Jin, Y. Sun, J. Xu, L. Liang, H. Ju, J. Zhu, Y. Pan and W. Yan, *JACS,* 2017, **139**, 18044-18051.
18. A. Ñlvarez, M. Borges, J. J. Corral-Pérez, J. G. Olcina, L. Hu, D. Cornu, R. Huang, D. Stoian and A. Urakawa, *ChemPhysChem,* 2017, **18**, 3135-3141.
19. M. Pérez-Jiménez, H. Corona, F. De La Cruz-Martínez and J. Campos, *Chemistry–A European Journal,* 2023, **29**, e202301428.
20. A. M. Appel, J. E. Bercaw, A. B. Bocarsly, H. Dobbek, D. L. Dubois, M. Dupuis, J. G. Ferry, E. Fujita, R. Hille and P. J. Kenis, *Chem. Rev.,* 2013, **113**, 6621-6658.
21. X. Jin, Y. Xu, X. Zhou, C. Lv, Q. Huang, G. Chen, H. Xie, T. Ge, J. Cao and J. Zhan, *ACS Mater. Lett.,* 2021, **3**, 364-371.
22. M. K. Hussien, A. Sabbah, M. Qorbani, R. Putikam, S. Kholimatussadiah, D. L. M. Tzou, M. H. Elsayed, Y. J. Lu, Y. Y. Wang and X. H. Lee, *Small,* 2024, 2400724.
23. N. Q. Thang, A. Sabbah, R. Putikam, C. Y. Huang, T. Y. Lin, M. K. Hussien, H. L. Wu, M. C. Lin, C. H. Lee and K. H. Chen, *Advanced Functional Materials,* 2025, 2423751.
24. T. T. Mamo, M. Qorbani, A. G. Hailemariam, R. Putikam, C.-M. Chu, T.-R. Ko, A. Sabbah, C.-Y. Huang, S. Kholimatussadiah and T. Billo, *Nano Energy,* 2024, **128**, 109863.
25. S.-M. Chang and W.-S. Liu, *Appl. Catal., B,* 2011, **101**, 333-342.
26. H. Pan, M. Sun, X. Wang, M. Zhang, M. Murugananthan and Y. Zhang, *Applied Catalysis B: Environment and Energy,* 2022, **307**, 121174.
27. J. Li, M. Zhang, Z. Guan, Q. Li, C. He and J. Yang, *Appl. Catal., B,* 2017, **206**, 300-307.
28. Y. Pan, X. Wang, W. Zhang, L. Tang, Z. Mu, C. Liu, B. Tian, M. Fei, Y. Sun and H. Su, *Nat. Commun.,* 2022, **13**, 3063.
29. Z. Zhang, C. Feng, D. Wang, S. Zhou, R. Wang, S. Hu, H. Li, M. Zuo, Y. Kong and J. Bao, *Nat. Commun.,* 2022, **13**, 2473.
30. Y. Zhang, J. Zhao, H. Wang, B. Xiao, W. Zhang, X. Zhao, T. Lv, M. Thangamuthu, J. Zhang and Y. Guo, *Nat. Commun.,* 2022, **13**, 58.
31. W. Tu, Y. Xu, J. Wang, B. Zhang, T. Zhou, S. Yin, S. Wu, C. Li, Y. Huang and Y. Zhou, *ACS Sustain. Chem. Eng.,* 2017, **5**, 7260-7268.
32. Y. An, H. L. Li, Y. Y. Liu, B. B. Huang, Q. L. Sun, Y. Dai, X. Y. Qin and X. Y. Zhang, *Journal of Solid State Chemistry,* 2016, **233**, 194-198.
33. J. Yang, W. H. Li, K. Xu, S. Tan, D. Wang and Y. Li, *Angew Chem Int Ed Engl,* 2022, **61**, e202200366.
34. G. Wei, Z. Mao, L. Liu, T. Hao, L. Zhu, S. Xu, X. Wang and S. Tang, *ACS Appl. Mater. Interfaces,* 2024, **16**, 52233-52243.
35. Y. Q. Zhang, D. Wang, G. P. Wei, B. L. Li, Z. C. Mao, S. M. Xu, S. B. Tang, J. Jiang, Z. Y. Li, X. J. Wang and X. Xu, *JACS Au,* 2024, **4**, 1509-1520.
36. B. Hu, Z. Li, B. Wang, L. Chen, X. Wang, X. Hu, Z. Bai, Y. Li, G. Chen and X. Luo, *Appl. Catal. B Environ.,* 2025, **371**, 125196.
37. H. Shi, H. Wang, Y. Zhou, J. Li, P. Zhai, X. Li, G. G. Gurzadyan, J. Hou, H. Yang and X. Guo, *Angewandte Chemie,* 2022, **134**, e202208904.
38. P. Dong, G. Hou, X. Xi, R. Shao and F. Dong, *Environ. Sci.: Nano,* 2017, **4**, 539-557.
39. V. Dutta, S. Sharma, P. Raizada, V. K. Thakur, A. a. P. Khan, V. Saini, A. M. Asiri and P. Singh, *J. Environ. Chem. Eng. ,* 2021, **9**, 105018.
40. X. Zhang, H. Su, P. Cui, Y. Cao, Z. Teng, Q. Zhang, Y. Wang, Y. Feng, R. Feng and J. Hou, *Nat. Commun.,* 2023, **14**, 7115.
41. S. H. Talib, S. Hussain, S. Baskaran, Z. Lu and J. Li, *ACS Catal.,* 2020, **10**, 11951-11961.
42. L. Liang, X. Li, Y. Sun, Y. Tan, X. Jiao, H. Ju, Z. Qi, J. Zhu and Y. Xie, *Joule,* 2018, **2**, 1004-1016.
43. J. Guo, H. Liu, D. Li, J. Wang, X. Djitcheu, D. He and Q. Zhang, *RSC Adv.,* 2022, **12**, 9373-9394.
44. H. Zhang, Y. Wang, S. Zuo, W. Zhou, J. Zhang and X. W. D. Lou, *JACS,* 2021, **143**, 2173-2177.
45. A. Sabbah, I. Shown, M. Qorbani, F.-Y. Fu, T.-Y. Lin, H.-L. Wu, P.-W. Chung, C.-I. Wu, S. R. M. Santiago and J.-L. Shen, *Nano Energy,* 2022, **93**, 106809.
46. F.-Y. Fu, C.-C. Fan, M. Qorbani, C.-Y. Huang, P.-C. Kuo, J.-S. Hwang, G.-J. Shu, S.-M. Chang, H.-L. Wu and C.-I. Wu, *Sustainable Energy & Fuels,* 2022, **6**, 4418-4428.
47. G. Kresse and J. Furthmüller, *Phys. Rev. B,* 1996, **54**, 11169.
48. G. Kresse and D. Joubert, *Phys. Rev. B,* 1999, **59**, 1758.
49. J. P. Perdew, K. Burke and M. Ernzerhof, *Phys. Rev. Lett.,* 1996, **77**, 3865.
50. J. K. Nørskov, J. Rossmeisl, A. Logadottir, L. Lindqvist, J. R. Kitchin, T. Bligaard and H. Jonsson, *The Journal of Physical Chemistry B,* 2004, **108**, 17886-17892.
51. L. I. Bendavid and E. A. Carter, *The Journal of Physical Chemistry C,* 2013, **117**, 26048-26059.
52. V. Wang, N. Xu, J.-C. Liu, G. Tang and W.-T. Geng, *Computer Physics Communications,* 2021, **267**, 108033.
53. M. Thommes, K. Kaneko, A. V. Neimark, J. P. Olivier, F. Rodriguez-Reinoso, J. Rouquerol and K. S. Sing, *Pure Appl. Chem.,* 2015, **87**, 1051-1069.
54. J. Klein, L. Kampermann, B. Mockenhaupt, M. Behrens, J. Strunk and G. Bacher, *Adv Funct Mater,* 2023, **33**, 2304523.
55. H. Yang, H. Sun, Q. Li, P. Li, K. Song, B. Song and L. Wang, *Vacuum,* 2019, **164**, 411-420.
56. M. Gillet, K. Aguir, C. Lemire, E. Gillet and K. Schierbaum, *Thin Solid Films,* 2004, **467**, 239-246.
57. A. Boubnov, A. Roppertz, M. D. Kundrat, S. Mangold, B. Reznik, C. R. Jacob, S. Kureti and J.-D. Grunwaldt, *Appl. Surf. Sci.,* 2016, **386**, 234-246.
58. K. Pandya, W. O'grady, D. Corrigan, J. Mcbreen and R. Hoffman, *J. Phys. Chem.,* 1990, **94**, 21-26.
59. C. Zhong, Y. Xu, X. Wu, S. Yin, X. Zhang, L. Zhou and H. You, *Adv. Mater.,* 2024, **36**, 2309500.
60. T. J. Frankcombe and Y. Liu, *Chem. Mater.,* 2023, **35**, 5468-5474.
61. D. K. Dogutan and D. G. Nocera, *Accounts Chem Res,* 2019, **52**,

View Article Online
DOI: 10.1039/D5TA10187E

3143-3148.
62. W. Tang, E. Sanville and G. Henkelman, *J. Phys.: Condens. Matter,* 2009, **21**, 084204.
63. B. M. Abraham, O. Piqué, M. A. Khan, F. Viñes, F. Illas and J. K. Singh, *ACS Appl. Mater. Interfaces,* 2023, **15**, 30117-30126.
64. X. Li, Y. Li, P. Li, D. Yuan, Y. Fu, J. Huang, Y. Fang, F. Wang, M. Anpo and L. Tan, *Molecular Catalysis,* 2025, **585**, 115356.
65. J. D. Yi, R. Xie, Z. L. Xie, G. L. Chai, T. F. Liu, R. P. Chen, Y. B. Huang and R. Cao, *Angewandte Chemie,* 2020, **132**, 23849-23856.

View Article Online
DOI: 10.1039/D5TA10187E

Data availability

The data supporting this article have been included as part of the Supplementary Information.

Supplementary information: Fig. S1-S17 and Tables S1-S11.